Structural, vibrational, and thermochemical properties of the monazite-type solid solution $La_{1-x}Pr_xPO_4$

A. Hirsch

Institut für Kristallographie, RWTH Aachen University, D-52066 Aachen, Germany

P. Kegler

Institut für Energie- und Klimaforschung (IEK6), Forschungszentrum Jülich, D-52425 Jülich, Germany

I. Alencar[1]

Institut für Geowissenschaften, Johann Wolfgang Goethe-Universität, D-60438 Frankfurt am Main, Germany

J. Ruiz-Fuertes[2]

Institut für Geowissenschaften, Johann Wolfgang Goethe-Universität, D-60438 Frankfurt am Main, Germany

A. Shelyug

Peter A. Rock Thermochemistry Laboratory and NEAT OUR, University of California at Davis, Davis CA-95616, U.S.A.

L. Peters

Institut für Kristallographie, RWTH Aachen University, D-52066 Aachen, Germany

C. Schreinemachers

Institut für Energie- und Klimaforschung (IEK6), Forschungszentrum Jülich, D-52425 Jülich, Germany

A. Neumann[3]

Institut für Kristallographie, RWTH Aachen University, D-52066 Aachen, Germany

S. Neumeier

Institut für Energie- und Klimaforschung (IEK6), Forschungszentrum Jülich, D-52425 Jülich, Germany

H.-P. Liermann

Deutsches Elektronen-Synchrotron (DESY) Photon Science, D-22607 Hamburg, Germany

A. Navrotsky

Peter A. Rock Thermochemistry Laboratory and NEAT OUR, University of California Davis, Davis CA-95616, U.S.A.

G. Roth

Institut für Kristallographie, RWTH Aachen University, D-52066 Aachen, Germany

---

Abstract

The monazite-type solid solution $La_{1-x}Pr_xPO_4$ was synthesized by solid-state reaction and extensively investigated using electron microprobe and thermogravimetric analyses, differential scanning and high-temperature oxide melt solution calorimetry, powder X-ray diffraction, infrared and Raman spectroscopy. Lattice parameters and *Ln*-O bond lengths show a decrease with increasing Pr content. A small excess volume is observed for the solid solution. IR spectra of the solid solution members present no detectable differences, while a blue shift of the PO_4-related modes is seen in the Raman data. This shift can be attributed to the lanthanide contraction. Within errors, calorimetry data show no systematic deviation from an ideal behavior, though one might interpret the data as an indication of a slightly asymmetric mixture. All data indicate that deviations from ideality of the solid solution – if present – are very small.

Keywords: Monazite, Rare earth phosphate, Solid solution, Powder X-ray diffraction, Raman spectroscopy, Calorimetry, Enthalpy of mixing

1. Introduction

Monazite has been investigated for more than six decades for numerous reasons, ranging from potential technical applications as luminophors or lasers [1, 2, 3] to geochronological studies [4, 5, 6, 7, 8, 9]. It is an important source for thorium, lanthanum and cerium and proposed as a host matrix for long term storage of high-level radioactive nuclear waste [10, 11, 12, 13, 14, 15, 16, 17, 18, 19, 20, 21, 22, 23, 24]. The immobilization of nuclear waste is a pressing topic in the context of deep geological final repositories. An optimal waste form must be chemically durable against alteration due to reactions with groundwater [e.g. 25, 26, 27]) and it must be able to withstand the cumulative radiation damage produced by the decay of the radioactive nuclei and the environmental conditions in the repository without mechanical, chemical or structural disintegration [e.g. 11, 28, 29]. Mineralogical evidence suggests that monazite fulfills these requisites: monazite is occurring as an accessory mineral in granites, gneisses or alluvial fans and it is very flexible with respect to chemical substitution [20, 21, 23, 30]. Natural monazite can contain high amounts of tetravalent Th or U [12]. Despite the substantial incorporation of radioactive elements, monazite is mostly found in crystalline form rather than being metamict and recovering after self-annealing[24]. An expected amorphization due to accumulation of radiation damage is, in fact, observed at laboratory conditions. This is compensated for by the low critical temperature of amorphization (*i.e.* low recrystallization temperature), as was shown by ion-irradiation experiments [31, 32, 33, 34, 35, 36]. Some swelling caused by the retention of He had been reported [6, 7, 8]. These properties are the reason for the community's interest in monazite as a ceramic host matrix for the immobilization of long-lived radionuclides such as the minor actinides and Pu [24, 37, 38, 39]. Many studies partly use Ln^{3+} as surrogates for the minor actinides. The formation of solid solutions is essentially influencing these properties. Most of the published studies on $Ln\mathrm{PO}_4$ solid solutions were concerned with the phase transition between the monazite- and the xenotime-type structures (Ref. [30] and references therein). Both structures are rare earth orthophosphates, but while monazite incorporates La-Gd which are the lighter Ln ions, in xenotime, heavy Ln are incorporated [40, 41, 42, 43, 44, 45]. In the present study, we applied several analytical techniques to extensively characterize a monazite-type solid solution. Such broad investigations are rather scarce [46, 47, 48, 49, 50, 51, 52], and mostly on Ce, Gd or Eu concerning sintering behavior. We chose Pr to fill this knowledge gap. It was used as a surrogate for minor actinides. Its ionic radius (0.99 Å) is very close to Np^{3+} [1.01 Å 53] and their outer shell electron distribution is similar ($4f^35d^06s^2$ and $5f^46d^17s^2$, respectively, [50]. To investigate the influence of Pr substitution in $LaPO_4$ on structure and properties, we synthesized powder samples by solid state reaction and characterized them by electron probe micro analysis (EPMA) and thermogravimetric analysis (TGA) , differential scanning calorimetry (DSC), powder X-ray diffraction (PXRD), infrared (IR) and Raman spectroscopy, and high-temperature oxide melt solution calorimetry.

Email address: `hirsch@ifk.rwth-aachen.de` (A. Hirsch)

[1] Present address: Instituto de Física, Universidade Federal do Rio Grande do Sul, CEP 91501-970 Porto Alegre-RS, Brazil

[2] Present address: Departament de Física Aplicada - ICMUV, Universitat de València, E-46100 Burjassot, Spain

[3] Present address: Institut für Geowissenschaften Mineralogie / Geochemie und Geographie, Martin-Luther-Universität Halle-Wittenberg, D-06120 Halle (Saale), Germany

2. Materials and Methods

2.1. Synthesis

Powder samples of $La_{1-x}Pr_xPO_4$ were prepared by solid state reaction, essentially following the route described by Bregiroux et al [29]. The reactants were La_2O_3 (Rhône-Poulenc, 95 %), Pr_2O_3 (Sigma-Aldrich, 99.9 %) and $NH_4H_2PO_4$ (Alfa Aesar, 98 %).

For the *Ln* oxides, loss on ignition was determined at 1273 K. For ammonium hydrogen phosphate, an excess of 10 wt -% (with respect to a stoichiometric mixture) was used to account for the high vapor pressure of P_4O_{10} at elevated temperatures. The powders were homogenized, pelletized and heated in Al_2O_3 crucibles at 1523 K for 24 h at ambient atmosphere. Samples were prepared in molar steps of $\Delta x = 0.1$. For the calorimetric measurements, two additional Pr rich samples were prepared with $x = 0.85$ and $x = 0.95$.

2.2. Experimental methods

For chemical characterization, EPMA were performed on a *JEOL* JXA 8900R. The electron beam had a diameter of $1\,\mu\mathrm{m}$ and was operated at 20 kV acceleration voltage and 40 nA current. 15 different grains were analyzed for each composition. Calibration standards for P, La and Pr were $CePO_4$ (USNM 168484), $LaPO_4$ (USNM 168490) and $PrPO_4$ (USNM 168493), respectively (Smithsonian Institution, Washington) [54].

TGA and DSC were performed on a *Netzsch* STA 449 *F3 Jupiter* system to check for phase transitions and reactions. Approximately 30 mg of each sample were heated in a covered corundum crucible from room temperature to 1373 K at a rate of 10 K/min and kept at this temperature for 10 min before cooling down at the same rate. Corundum was used as reference material. The base line was corrected using an empty crucible.

Laboratory PXRD was performed at room temperature on a *PANalytical X' Pert Pro* diffractometer in Bragg-Brentano θ-θ-geometry to check phase purity. The system is equipped with Cu-tube and Ni-filter, yielding $\mathrm{Cu-K}_{\alpha 1,2}$ radiation, and an *X'Celerator* semiconductor strip detector. Measurements on flat samples were recorded in the 2θ range $10-110\,^\circ$ with a step-size of $\Delta 2\theta = 0.008^\circ$ for an acquisition time of 37 s per step. Synchrotron PXRD data for structural refinement were collected at the High Resolution Powder Diffraction Beamline P02.1 at PETRA III (DESY, Hamburg, Germany). The system is equipped with a $\mathrm{Si}(111)$ monochromator and a *PerkinElmer XRD1621* fast area detector. A wavelength of $\lambda = 0.207120$ Å was employed, using CeO_2 (*NIST 674b*) and Si (*NIST 640d*) as calibrants. Samples were placed in SiO_2-glass capillaries of 0.5 mm diameter. Measurements were recorded for 100 s under ambient conditions and at 100 K, spinning the sample capillaries. The sample-to-detector distance was determined from the Si data using *Fit2D* [55], which was also used for the integration of the two-dimensional diffraction data. Structure refinements were carried out against both, laboratory and synchrotron data, employing the Rietveld method [56] as implemented in the program *Topas Academic* [57]. In the refinement, a (6 to 12 coefficients) background polynomial, a modified pseudo-Voigt profile function [58], reflection asymmetry, sample height (for flat samples only), lattice parameters and fractional coordinates for all sites, as well as isotropic thermal displacement parameters for each atom were allowed to vary. The monazite structure published by Ni et al [40] was used as a starting model.

IR spectroscopy was performed on a *Bruker AXS EQUINOX 55* FT-IR spectrometer. Spectra were recorded in the wavenumber range of $4000 - 400\,\mathrm{cm}^{-1}$ with a resolution of $2\,\mathrm{cm}^{-1}$. For the measurements, 1 mg of sample was mixed with 250 mg KBr and pressed to pellets. These pellets were measured directly after preparation. The data was analyzed with *OriginPro* 9.0.0G [59].

Raman spectroscopy was recorded on a *Renishaw* RM-1000 spectrometer. The system is equipped with a $20\times$ objective and a 1800 grooves / mm grating, operating in quasi-backscattering geometry without polarization analysis. The exciting source was a Nd:YAG laser ($\lambda = 532$ nm wavelength, 2 mW output power on the sample) filtered by Notch filters. Spectra were recorded either in the wavenumber range of 100–$1200\,\mathrm{cm}^{-1}$ during 10 s or in static mode between 530–$1380\,\mathrm{cm}^{-1}$ for 10 accumulations of 1 s each. The resolution is $2\,\mathrm{cm}^{-1}$. Peak fitting including calculations of the full width at half maximum (FWHM) were carried out with *OriginPro* 9.0.0G [59].

High-temperature oxide melt solution calorimetry was performed using a custom-built Tian-Calvet-type twin calorimeter [60, 61, 62]. On both sides of the calorimeter, Pt-crucibles were filled with 20 g of sodium molybdate ($3\,Na_2O \cdot 4\,MoO_3$) each, which was used as the solvent at 973 K. The melt was stirred by "bubbling" [62] with oxygen (rate 5.9 ml/min) to assure oxidizing conditions. Bubbling also enhances the dissolution and prevents local saturation of the solvent [62]. Additionally, a constant flow of O_2 gas (40 ml/min) was flushed through the calorimeter chamber to generate a constant gas environment above the solvent and to remove any evolving gases. The calorimeter was calibrated by measuring the heat content of α-Al_2O_3 pellets. The calibration was cross checked by dropping a number of TiO_2 pellets (*in-house* standard).

Samples for the calorimetric measurements were thermally treated at 1073 K for at least 8 h to remove any water from the surface. For the measurement of the enthalpy of solution (ΔH_{ds}), approximately 5 mg of the sample were pressed to a cylindrical pellet and dropped into the solvent. 8-10 drops were measured per composition. The calorimetric curves returned to the baseline signal within thirty minutes, consistent with rapid sample dissolution. The heat-flow signal was integrated over time to determine H_{ds} using the software *Calisto SETARAM*. The achievable accuracy of ΔH_{ds} is in the range of ± 1 kJ/mol. By employing appropriate thermochemical cycles (Table 1), enthalpies of formation from oxides and elements as well as the enthalpy of mixing were calculated. A full description of the methodology has been published elsewhere [63].

3. Results and Discussion

3.1. Chemical and thermal characterization

EPMA revealed that the grains were not individual crystals but aggregates of micron-sized crystallites. The samples were highly porous (a picture of an exemplary sample can be found in the electronic supplemental material), probably due to the loss of NH_3 and H_2O during the synthesis. A higher synthesis temperature may have enhanced sintering of the sample and therefore porosity might have been reduced. Within 1σ, no deviation from the nominal composition was detected, indicating reasonable homogeneity of the samples: The molar ratios La/Pr varied as expected from the general formula $La_{1-x}Pr_xPO_4$, demonstrating that solid-state reaction can be used to synthesize homogeneous monazite solid solutions. In the following, compositions determined by EPMA were used in calculations, graphs, and tables.

Thermal characterization by TGA and DSC did not show any phase transitions or reactions. All samples showed similar behavior except for $PrPO_4$. This end member showed a slightly higher weight loss of about 1 % (0.30 mg) compared to the other samples. In an additional, second heating cycle, the mass stayed constant. We cannot exclude that this behavior is due to the loss of absorbed water or surplus P_4O_{10} (excess of $NH_4H_2PO_4$) in the first heating cycle or due to redox reactions of Pr^{3+}. However, structural analyses did not reveal any additional P or Pr phases (see chapter below).

3.2. Structural Characterization

High-resolution synchrotron data were used for refinement of the structural model proposed by Ni et al [40]. Further details of the crystal structure investigations may be obtained from FIZ Karlsruhe (on quoting the deposition numbers CSD-431743 to -431753 for $LaPO_4$ to $PrPO_4$). Monazite is a monoclinic orthophosphate (space group non-standard setting $P\,2_1/n$, $Z = 4$) with the generic formula LnPO$_4$. The Ln^{3+} cations (from La^{+3} to Gd^{+3}) are ninefold coordinated by O [64]. The main structural feature in monazite is alternating chains of edge-sharing LnO_9 polyhedra and PO_4 tetrahedra along the $\vec{c}$ axis (see Fig.1).

According to the diffraction patterns, the samples were single-phase monazite for all compositions. Figure 2 depicts a selected synchrotron Rietveld structure refinement of $La_{1-x}Pr_xPO_4$.

The lattice parameters decrease linearly with increasing Praseodymium content, while the monoclinic angle β increases (Fig. 3 left). Due to the smaller radius of Pr^{3+} (1.179 Å) compared to La^{3+} (1.216 Å) [53], this behavior could qualitatively be anticipated. The unit cell volume (Fig. 3 middle) shows a small deviation from linearity (and hence, Vegard's Law [65]). This was previously reported for $La_{1-x}Ln_xPO_4$ solid solutions [46, 66, 47].

The excess volume (inset in Figure 3 middle) is attributed to non-ideal mixing / strain effects caused by the different size of the *Ln* cations. Both, symmetric and asymmetric excess functions gave comparable fits with the maximum at $0.5 \leq x \leq 0.6$. Since the excess volume is very small (0.14 %), we cannot exclude any one of the models.

Within experimental uncertainty, the P-O bond lengths stay virtually constant (1.55 ± 0.02 Å), in good agreement with the sum of the individual ionic radii (1.56 Å from Shannon [53], inset in Fig. 3 on the right). An angular distortion of the PO_4 tetrahedron is observed for all compositions studied: three O–P–O angles are larger (up to 116.1±5°), and three O–P–O angles are smaller (down to 101.8±3°) than the ideal intratetrahedra angle (109.5°). This is due to Coulomb repulsions arising between the Ln^{3+} and P^{5+} atom which both share two O atoms along the

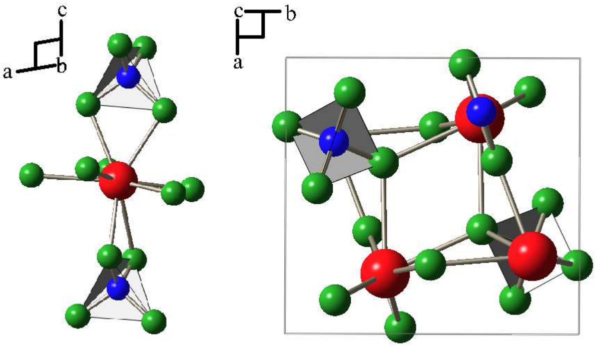

Figure 1: Crystal structure of monoclinic *Ln*-monazite-type orthophosphate after Ni et al [40]. Red: Ln^{3+}, blue: P^{5+}, green: O^{2-}, respectively. In gray: PO_4 tetrahedra. On the left: Chain structure formed by LnO_9 and PO_4 polyhedra; on the right: View of the unit cell along the [001] direction.

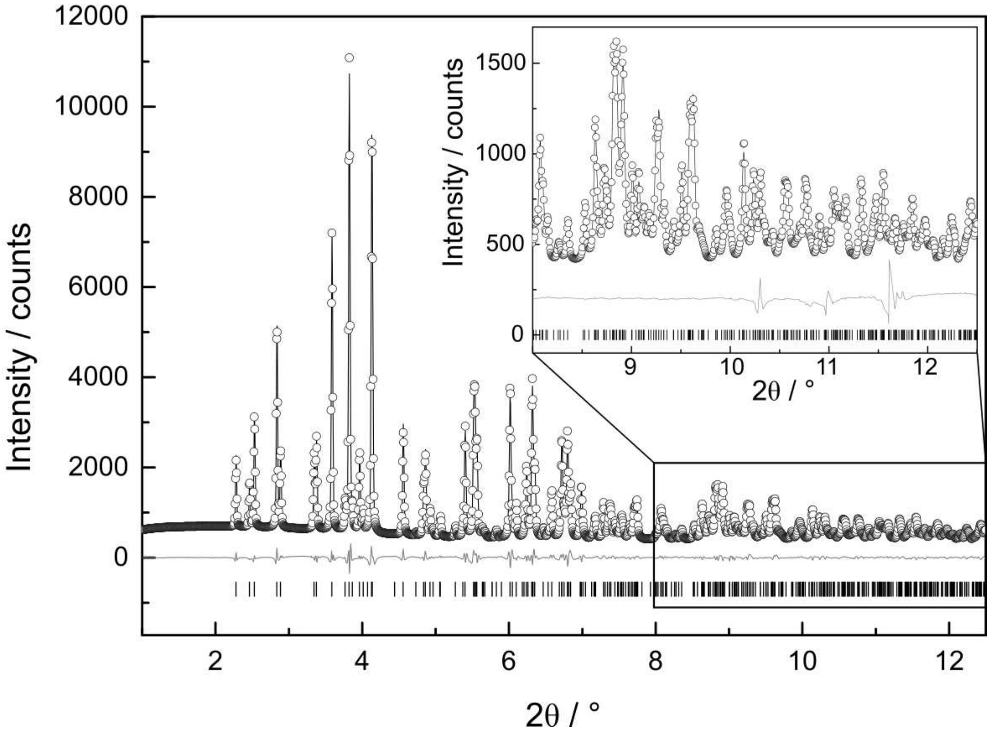

Figure 2: Rietveld plot of $La_{0.5}Pr_{0.5}PO_4$, synchrotron data, $\lambda = 0.207120$ Å. Open circles: measured intensity, black line: calculated intensity; gray: difference curve. Vertical lines: tic-marks for the position of calculated peaks for monazite [40]. Inset shows the 2θ range 8-12.5 °.

chain structure of monazite which is yielding a shorter O-O edge length. While in principle this angular distortion is known for various monazites [64, 67, 68, 69], no significant compositional trend can be read from our data within error bars. Hence, in a first approximation, the PO_4 tetrahedron can be considered as a rigid body. However, a significant decrease of the average *Ln*-O bond length is observed with increasing Pr-content (Fig. 3 right). Generally, the average distance is shorter than the sum of the average ionic radii[53] (2.596 Å and 2.559 Å for La-O and Pr-O, respectively) indicating some covalent bonding character.

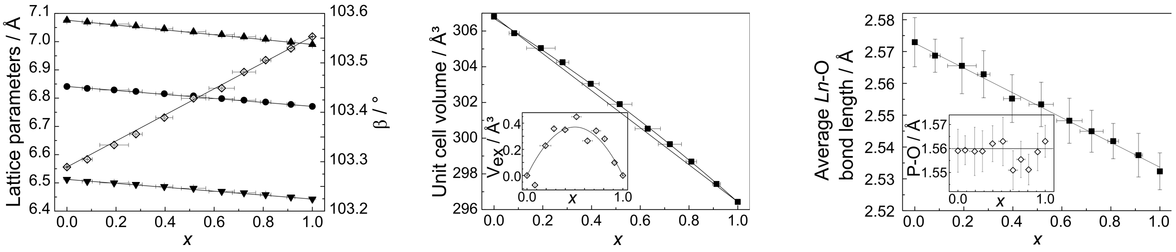

Figure 3: PXRD results for $La_{1-x}Pr_xPO_4$ as a function of x (Pr molar fraction) for different parameters: (Left) Lattice parameters a (circles), b (up-pointing triangles) and c (down-pointing triangles), and the monoclinic angle β (open diamonds). (Middle) Unit-cell volume and as an inset excess volume. (Right) Averaged *Ln*-O bond-length and as an inset averaged P-O bond length. Solid lines in all figures are guides to the eye, while in some cases error bars are smaller than the symbols.

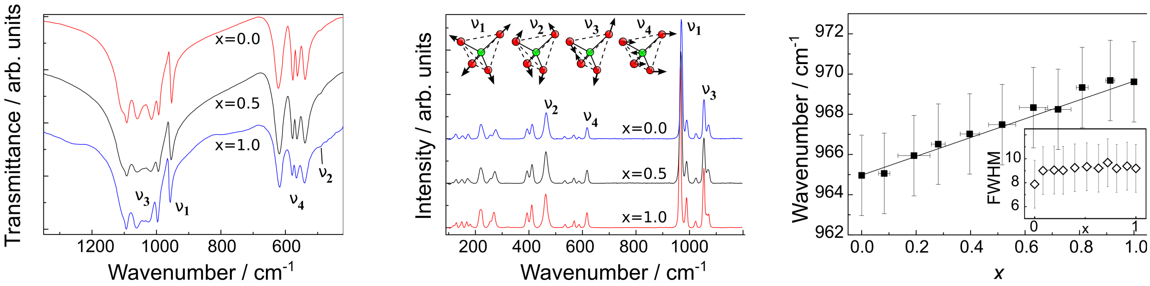

Figure 4: Vibrational spectra for $La_{1-x}Pr_xPO_4$: (Left) Typical IR spectra. (Middle) Typical Raman spectra. The insets represent the PO_4 symmetric or asymmetric stretching and bending modes. Note that the spectra are stacked for the sake of clarity. (Right) Wavenumber of the ν_1 mode for $La_{1-x}Pr_xPO_4$ as a function of x (Pr molar fraction) with the solid line as a guide to the eye and as an inset the full-width at half maximum (FWHM in cm^{-1}) of this line. In some cases error bars are smaller than data points.

3.3. *Vibrational spectroscopy*

Figure 4 (left) presents IR spectra of three $La_{1-x}Pr_xPO_4$ compositions while only the range is shown that is influenced by PO_4 modes of monazite. Spectra for all compositions are qualitatively comparable and available in the on-line supporting material. All IR active vibrations related to stretching and bending of the phosphate group[70] were observed. A broad band between 1094-993 cm^{-1} and a sharper band at 957-953 cm^{-1} can be assigned to asymmetric (ν_3) and symmetric (ν_1) stretching modes, respectively. The asymmetric bending modes (ν_4) are located between 621-538 cm^{-1}, while the symmetric bending mode (ν_2) only appears as a small shoulder of ν_4. Due to the limited resolution, its position ($\sim$ 488 cm^{-1}) is difficult to render more precisely. At higher wavenumbers, the vibrational modes of H_2O and CO_2 molecules are visible. These modes can be explained by the presence of these molecules in air and due to adsorption on the sample surface and on KBr which is known for its hygroscopic character. Within experimental resolution, none of the IR modes show a dependence on x.

Raman spectra for the same compositions as mentioned above are depicted in Figure 4 (middle). According to factor group analysis, 36 Raman active modes are allowed. 16 of those could be assigned unambiguously. The most intense modes are those related to the phosphate group.

After background removal, a pseudo-Voigt function was used to model each mode. The ν_1, ν_2, ν_3 and ν_4 vibrations are observed between 960-975 cm^{-1}, 460-470 cm^{-1}, 1050-1060 cm^{-1} and 615-625 cm^{-1}, respectively. These four modes show a linear increase of the wavenumber with increasing Pr content, as shown for the ν_1 mode in figure 4 (right).

Although this blue shift was already reported previously [71, 47], its origin is still a matter of debate [72]. On the one hand [73, 74], a compression of the PO_4 tetrahedron in terms of shorter P-O distances is proposed, resulting in a denser packing of polyhedra. On the other hand [75, 76], the blue shift is attributed to a bond length contraction at the *Ln* site, in terms of shorter *Ln*-O distances. X-ray diffraction data from this work show that (within resolution) the

P-O bond lengths remain constant, while the *Ln*-O distances decrease. Hence, it appears more obvious that the blue shift originates in a contraction on the *Ln* site.

For the sake of completeness, the full-width at half maximum (*FWHM*) for the series is given in the inset in figure 4 (right). Apart from sharper bands in $\mathrm{LaPO_4}$ (probably due to the high porosity of the samples and therefore the poor focusing), the *FWHM* does not change significantly with composition.

3.4. High-temperature solution calorimetry

High-temperature solution calorimetry on $\mathrm{La}_{1-x}\mathrm{Pr}_x\mathrm{PO}_4$ was used to determine enthalpies of formation from the oxides ($\Delta H^\circ_{\mathrm{f,ox}}$) and from the elements ($\Delta H^\circ_{\mathrm{f,el}}$) as well as the enthalpy of mixing (ΔH_{mix}) for the solid solution (see Table 2). The calorimeter measures the heat-flow of a sample which is dropped into a molten oxide solvent at a constant temperature (isoperibol setup) [60, 61, 62]. The heat-flow consists of the heating up of the sample to 973 K and the dissolution of the sample in the solvent, as well as possible changes in the valence state of the dissolved compounds. Since Pr is known for its affinity to higher valence states at oxidizing conditions, the oxidation of Pr^{+3} in the solvent was accounted for in the thermochemical cycle (see Table 1). Ushakov et al [63] showed that $\mathrm{PrO}_{1.83}$ is the stable species of Pr in the solvent because of the oxidation of Pr^{3+} to $\mathrm{Pr}^{3.66+}$ in the solvent. For the calculation of the formation enthalpy from the oxides ($\Delta H(10)$), several steps are required as shown in Tab. 1. At first, the enthalpy of dissolution of $\mathrm{PrO}_{1.83}$ (ΔH_{ds} $\mathrm{PrO}_{1.83}$, $\Delta H(3)$) needs to be determined. Then the energy needed to heat oxygen to the calorimeter temperature ($\Delta H_{298-973}$ O_2, $\Delta H(4)$) is subtracted from the first part. Finally, the difference between the elemental enthalpy of formation of $\mathrm{PrO}_{1.83}$ (ΔH^0_f $\mathrm{PrO}_{1.83}$, $\Delta H(7)$) and half a formula unit of elemental enthalpy of formation $\mathrm{Pr_2O_3}$ (ΔH^0_f $\mathrm{Pr_2O_3}$, $\Delta H(6)$) is calculated, which is added. This equals $\Delta H(3)$ - 0.165 $\Delta H(4)$ + $\Delta H(7)$ - 0.5 $\Delta H(6)$. This calculation is simalar to that by Ushakov et al. [63] for $\mathrm{CePO_4}$ which shows an oxidation form Ce^{3+} to Ce^{4+} in the solvent.

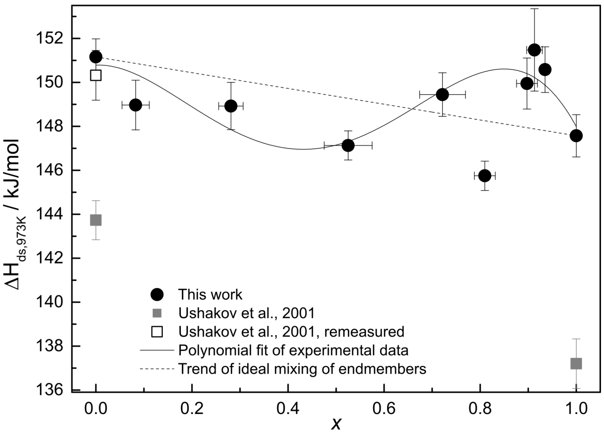

Figure 5: Enthalpy of solution ΔH_{ds} at 973 K versus Pr concentration (x) in the solid solution $\mathrm{La}_{1-x}\mathrm{Pr}_x\mathrm{PO}_4$. Where not visible, error bars are smaller than the symbols used.

The measured enthalpy of solution is shown in Fig. 5. A straight, dotted line indicates ideal mixing behavior, a polynomial fit (to our data points except the one for $x = 0.81$) of forth order is also given. Thermochemically, a 2nd order polynomial would be reasonable. With regard to the scattering of our data around the trend of an ideal solid solution, we chose the polynomial of the lowest order which gave an acceptable fit. The original values for pure La and Pr monazite [63] are included, and they show a clear deviation from our results. Fortunately, it was possible to remeasure Ushakov's $\mathrm{LaPO_4}$ sample with our set-up. The obtained value is in very good agreement with our $\mathrm{LaPO_4}$. Several samples of $\mathrm{PrPO_4}$ were synthesized following the route described in the synthesis section. Accidentally, a $\mathrm{PrPO_4}$ sample containing a $\mathrm{PrP_3O_9}$ impurity phase was used for calorimetric measurements in the initial experiments, giving a result identical to the original value of Ushakov et al [63]. A heat-treatment at 1773 K for 12 h eliminated the phosphorous excess phase. After checking purity by PXRD, the stated enthalpy of solution was obtained for $\mathrm{PrPO_4}$ (Fig. 5). This resulted in an almost linear trend for the whole solid solution. It may be that the sample used

Table 1: Thermochemical cycle for the determination of enthalpy of formation of $La_{1-x}Pr_xPO_4$ solid solution from oxides and elements. The subscripts correspond to: s = solid, 298 = 298 K, 973 = 973 K, sln = solution, ds = (drop) solution, cr = crystalline, g = gaseous. (a from [77], b from [63], c from [78], d was calculated as a theoretical ΔH_{ds} Pr_2O_3)

Reaction			ΔH[kJ/mol]
$La_{1-x}Pr_xPO_{4(s,298)}$ + x 0.165 $O_{2(g,298)}$ $\rightarrow$ 0.5 (1-x) $La_2O_{3(sln,973)}$ + x $PrO_{1.83(sln,973)}$ + 0.5 $P_2O_{5(sln,973)}$	(1)	ΔH_{ds} $La_{1-x}Pr_xPO_4$	see table 2
$La_2O_{3(cr,298)} \rightarrow La_2O_{3(sln,973)}$	(2)	ΔH_{ds} La_2O_3	-225.1 ± 3.16[a]
$PrO_{1.83(cr,298)} \rightarrow PrO_{1.83(sln,973)}$	(3)	ΔH_{ds} $PrO_{1.83}$	-41.6 ± 1.0[b]
$O_{2(g,298)} \rightarrow O_{2(g,973)}$	(4)	$\Delta H_{(298-973)}$ O_2	21.7[c]
$P_2O_{5(cr,298)} \rightarrow P_2O_{5(sln,973)}$	(5)	ΔH_{ds} P_2O_5	-164.6 ± 0.5[b]
2 $Pr_{(s,298)}$ + 1.5 $O_{2(g,298)} \rightarrow Pr_2O_{3(s,298)}$	(6)	ΔH^0_f Pr_2O_3	-1809.6 ± 6.7[c]
$Pr_{(s,298)}$ + 0.915 $O_{2(g,298)} \rightarrow PrO_{1.83(s,298)}$	(7)	ΔH^0_f $PrO_{1.83}$	-952.3 ± 3.4[c]
2 $La_{(s,298)}$ + 1.5 $O_{2(g,298)} \rightarrow La_2O_{3(s,298)}$	(8)	ΔH^0_f La_2O_3	-1791.6 ± 1.6[c]
2 $P_{(s,298)}$ + 2.5 $O_{2(g,298)} \rightarrow P_2O_{5(s,298)}$	(9)	ΔH^0_f P_2O_5	-1504 ± 0.5[c]
0.5 (1-x) $La_2O_{3(s,298)}$ + 0.5 x $Pr_2O_{3(s,298)}$ + 0.5 $P_2O_{5(s,298)}$ $\rightarrow$ $La_{1-x}Pr_xPO_{4(s,298)}$	(10)	$\Delta H^0_{f,ox}$ $La_{1-x}Pr_xPO_4$	see table 2
$\Delta H(10)$ = -$\Delta H(1)$ + 0.5 (1-x) $\Delta H(2)$ + $x(\Delta H(3)$ - 0.165 $\Delta H(4)$ + $\Delta H(7)$ - 0.5 $\Delta H(6))$ + 0.5 $\Delta H(5)$			
(1-x) $La_{(s,298)}$ + x $Pr_{(s,298)}$ + $P_{(s,298)}$ + 2 $O_{2(g,298)} \rightarrow La_{1-x}Pr_xPO_{4(s,298)}$	(11)	$\Delta H^0_{f,el}$ $La_{1-x}Pr_xPO_4$	see table 2
$\Delta H(11)$ = 0.5 (1-x) $\Delta H(8)$ + 0.5 x $\Delta H(6)$ + 0.5 $\Delta H(9)$ + $\Delta H(10)$			

Table 2: Enthalpies of solution ($\Delta H_{\mathrm{ds},973K}$) in $3\,\mathrm{Na_2O}\cdot 4\,\mathrm{MoO_3}$ at 973 K as a function of molar fraction of Pr (x) in solid solution and number of measurements (n), enthalpies of formation from oxides ($\Delta H^\circ_{\mathrm{f,ox}}$) and elements ($\Delta H^\circ_{\mathrm{f,el}}$) at 298 K, and enthalpy of mixing (ΔH_{mix}) for $\mathrm{La}_{1-x}\mathrm{Pr}_x\mathrm{PO}_4$ solid solution. All enthalpies in kJ/mol.

x	n	$\Delta H_{\mathrm{ds},973}$	$\Delta H^\circ_{\mathrm{f,ox}}$	$\Delta H^\circ_{\mathrm{f,el}}$	ΔH_{mix}
0.00 ± 0.00	10	151.13 ± 2.30	-346.01 ± 3.92	-1994.26 ± 4.25	—
0.08 ± 0.03	8	148.97 ± 1.13	-342.18 ± 3.26	-1991.17 ± 4.10	-1.90 ± 1.27
0.28 ± 0.03	9	148.92 ± 1.08	-338.20 ± 2.96	-1988.98 ± 4.83	-1.23 ± 1.29
0.53 ± 0.05	8	147.13 ± 0.66	-331.56 ± 2.42	-1984.54 ± 5.54	-2.14 ± 1.12
0.72 ± 0.05	8	149.44 ± 0.99	-329.98 ± 2.16	-1984.73 ± 6.15	$+0.87 \pm 1.44$
0.81 ± 0.02	9	145.75 ± 0.67	-324.54 ± 1.83	-1980.08 ± 6.34	-2.50 ± 1.29
0.90 ± 0.02	6	149.95 ± 1.16	-327.00 ± 1.86	-1983.33 ± 6.63	$+2.01 \pm 1.65$
0.91 ± 0.02	8	151.48 ± 1.87	-328.22 ± 2.34	-1984.69 ± 6.83	$+3.59 \pm 2.21$
0.94 ± 0.00	8	150.58 ± 1.04	-326.88 ± 1.69	-1983.55 ± 6.71	$+2.78 \pm 1.59$
1.00 ± 0.00	8	147.57 ± 0.96	-322.59 ± 1.46	-1979.84 ± 6.86	—

by Ushakov et al [63] probably contained the same impurity phase and hence, showed the same behavior as our contaminated $\mathrm{PrPO_4}$ sample.

The enthalpy of mixing as given in Table 2 was determined as the deviation of the measured enthalpies of solution from ideal behavior (dotted line connecting the end-members in Fig. 5). Within experimental uncertainties, no deviation from ideal behavior can be statistically confirmed. However, neglecting the data point for $x = 0.81$, a 4$^{\mathrm{th}}$ order polynomial resulted in the best fit ($R^2 = 0.63$) as shown in Fig. 5 as a solid line. It might be that *e.g.* a minor impurity phase ($\ll 2$ wt%) as observed for the $\mathrm{PrPO_4}$ sample measured first could lead to the observed misfit of this particular data point. In this case, such a phase was possibly below the detection limit of the PRXD and EPMA measurements, but sufficient to bias calorimetric data. In that case, $\mathrm{La}_{1-x}\mathrm{Pr}_x\mathrm{PO}_4$ could be interpreted as a slightly non-ideal solid solution as suggested by the polynomial fit in Fig. 5. Anyhow, the deviation from the ideal behavior is not of the order of magnitude to assume a miscibility gap. The absence of such a miscibility gap is confirmed throughout this extensive investigation.

4. Summary and conclusions

A monazite $\mathrm{La}_{1-x}\mathrm{Pr}_x\mathrm{PO}_4$ solid solution was successfully synthesized by solid-state reaction. Chemical, thermal and structural analyses confirm chemical and phase purity. From diffraction, the $\mathrm{PO_4}$ polyhedron is interpreted as slightly distorted, but a rigid tetrahedron, and the $Ln\mathrm{O_9}$ polyhedron contracts due to the lanthanide contraction. While IR spectra do not significantly change with composition, Raman spectra clearly demonstrate a blue shift of the $\mathrm{PO_4}$ related modes. This could be attributed to a stiffening of P–O-bonds due to stronger *Ln*–O-interactions. This result substantiate the advantage of combining global, long-range (diffraction) and local, short-range (spectroscopy) methods for extensive structural investigations. Drop solution calorimetric measurements yield a consistent set of solution enthalpies for $\mathrm{La}_{1-x}\mathrm{Pr}_x\mathrm{PO}_4$, thereby correcting published data for the end-members [63]. The results once again emphasize the importance of phase-pure material for calorimetry. This is, however, a matter of the detection limits of the methods used for prior characterization.

The extensive investigation reported here shows that $\mathrm{La}_{1-x}\mathrm{Pr}_x\mathrm{PO}_4$ constitutes an almost ideal solid solution without a clear evidence for a miscibility gap. Thermodynamically stable solid solutions without miscibility gaps are crucial prerequisites for their use in nuclear waste management. It is also most likely that the advantageous properties of the monazite end-members (like high aqueous insolubility, waste loading and radiation tolerance [19]) can be expected for the whole solid solution.

Acknowledgements

A.H. gratefully thanks the Federal Ministry of Education and Research (BMBF) for funding (02NUK021E). I.A. and J.R.-F., respectively, acknowledge the Brazilian National Council for Scientific and Technological Development (CNPq, Grant No. 237039/2012-5) and Alexander von Humboldt Foundation for post-doctoral fellowships. Calorimetry at UC Davis was supported by the Office of Basic Energy Sciences of the U.S. Department of Energy as part of the Materials Science of Actinides Energy Frontiers Research Center (DESC0001089). DESYPhoton Science is gratefully acknowledged for facilitate beam time. PETRA III at DESY is a member of Hermann von Helmholtz-Gemeinschaft Deutscher Forschungszentren (HGF). For additional sample preparation, we would like to thank Laura Ritterbach and Christa Claßen, as well as Nico Küter for the preparation of the samples for EPMA. IR measurements were kindly performed by Zaina Paparigas and Hildegard Curtius, and EPMA was discussed with Barbara Mader and Peter Appel.

References

[1] N. Hashimoto, Y. Takada, K. Sato, S. Ibuki, Green-luminescent (La,Ce)PO$_4$: Tb phosphors for small size fluorescent lamps, J. Lumin. 48 (1991) 893–897. `doi:doi:10.1016/0022-2313(91)90265-W`.

[2] P. Iacconi, M. Junker, B. Guilhot, D. Huguenin, Thermoluminescence of a mixed rare earth phosphate powder La$_{1-x-y}$ Ce$_x$ Tb$_y$ PO$_4$, Opt. Mater. 17 (3) (2001) 409–414.

[3] H. Dong, Y. Liu, P. Yang, W. Wang, J. Lin, Controlled synthesis and characterization of LaPO$_4$, LaPO$_4$: Ce^{3+} and LaPO$_4$: Ce^{3+}, Tb^{3+} by EDTA assisted hydrothermal method, Solid State Sci. 12 (9) (2010) 1652–1660.

[4] J.-M. Montel, S. Foret, M. Veschambre, C. Nicollet, A. Provost, Electron microprobe dating of monazite, Chem. Geol. 131 (1) (1996) 37–53.

[5] K. Suzuki, M. Adachi, Precamrbian provenance and Silurian metamorphism of the Tsubonosawa paragneiss in the South Kitakami terrane, Northeast Japan, revealed by the chemical Th–U–total Pb isochron ages of monazite, zircon and xenotime, Geochem. J. 25 (1991) 357–376.

[6] A. M. Seydoux-Guillaume, R. Wirth, L. Nasdala, M. Gottschalk, J. M. Montel, W. Heinrich, An XRD, TEM and Raman study of experimentally annealed natural monazite, Phys. Chem. Miner. 29 (4) (2002) 240–253. `doi:10.1007/s00269-001-0232-4`.

[7] A.-M. Seydoux-Guillaume, R. Wirth, A. Deutsch, U. Schärer, Microstructure of 24-1928 Ma concordant monazites; implications for geochronology and nuclear waste deposits, Geochim. Cosmochim. Acta 68 (11) (2004) 2517–2527.

[8] A.-M. Seydoux-Guillaume, J.-M. Montel, B. Bingen, V. Bosse, P. Parseval, J.-L. Paquette, E. Janots, R. Wirth, Low-temperature alteration of monazite: Fluid mediated coupled dissolution-precipitation, irradiation damage, and disturbance of the U–Pb and Th–Pb chronometers, Chem. Geol. 330–331 (2012) 140–158.

[9] B. Rasmussen, I. R. Fletcher, J. R. Muhling, In situ U–Pb dating and element mapping of three generations of monazite: unravelling cryptic tectonothermal events in low-grade terranes, Geochim. Cosmochim. Acta 71 (3) (2007) 670–690.

[10] L. Boatner, G. Beall, M. Abraham, C. Finch, P. Huray, M. Rappaz, Monazite and other lanthanide orthophosphates as alternate actinide waste forms, in: Scientific basis for nuclear waste management, Springer, 1980, pp. 289–296.

[11] R. C. Ewing, R. Haaker, The metamict state: Implications for radiation damage in crystalline waste forms, Nucl. Chem. Waste Man. 1 (1) (1980) 51–57.

[12] R. Ewing, W. Weber, F. Clinard, Radiation effects in nuclear waste forms for high-level radioactive waste, Prog.Nucl.Energ. 29 (2) (1995) 63–127.

[13] R. C. Ewing, Nuclear waste forms for actinides, P. Natl. Acad. Sci. USA 96 (7) (1999) Natl Acad Sci. `doi:10.1073/pnas.96.7.3432`.

[14] R. C. Ewing, L. M. Wang, Phosphates as nuclear waste forms, Rev. Mineral. Geochem. 48 (2002) Mineral Soc. Amer. `doi:10.2138/rmg.2002.48.18`.

[15] R. C. Ewing, Ceramic matrices for plutonium disposition, Prog.Nucl.Energ. 49 (8) (2007) 635–643. `doi:10.1016/j.pnucene.2007.02.003`.

[16] B. C. Sales, C. W. White, L. A. Boatner, A Comparison of the Corrosion Characteristics of Synthetic Monazite and Borosilicate Glass Containing Simulated Nuclear Defense Waste, Nucl. Chem. Waste Man. 4 (4) (1983) 281–289. `doi:10.1016/0191-815X(83)90053-0`.

[17] W. J. Weber, R. C. Ewing, C. R. A. Catlow, T. D. de la Rubia, L. W. Hobbs, C. Kinoshita, H. Matzke, A. T. Motta, M. Nastasi, E. K. H. Salje, E. R. Vance, S. J. Zinkle, Radiation effects in crystalline ceramics for the immobilization of high-level nuclear waste and plutonium, J. Mater. Res. 13 (6) (1998) 1434–1484. `doi:10.1557/JMR.1998.0205`.

[18] W. J. Weber, A. Navrotsky, S. Stefanovsky, E. R. Vance, E. Vernaz, Materials Science of High-Level Nuclear Waste Immobilization, MRS Bull. 34 (1) (2009) 46–53. `doi:10.1557/mrs2009.12`.

[19] G. R. Lumpkin, Ceramic waste forms for actinides, Elements 2 (6) (2006) 365–372. `doi:10.2113/gselements.2.6.365`.

[20] N. Dacheux, N. Clavier, R. Podor, Monazite as a promising long-term radioactive waste matrix: Benefits of high-structural flexibility and chemical durability, Am. Mineral. 98 (2013) 833–847.

[21] H. Schlenz, J. Heuser, A. Neumann, S. Schmitz, D. Bosbach, Monazite as a suitable actinide waste form, Z. Kristallogr. 228 (3) (2013) 113–123.

[22] G. Deissmann, S. Neumeier, G. Modolo, D. Bosbach, Durability of potential plutonium waste forms under repository conditions, Mineral. Mag. 76 (8) (2012) 2911–2918.

[23] L. A. Boatner, Synthesis, structure, and properties of monazite, pretulite, and xenotime, Rev. Mineral. Geochem. 48 (2002) Mineral Soc Amer. `doi:10.2138/rmg.2002.48.4`.

[24] L. Boatner, B. Sales, Monazite, in: W. Lutze, R. Ewing (Eds.), Radioactive waste forms for the future, Elsevier Science Publishers B.V., 1988, pp. 495–564.

[25] E. Veilly, E. Du Fou de Kerdaniel, J. Roques, N. Dacheux, N. Clavier, Comparative behavior of britholites and monazite/brabantite solid solutions during leaching tests: a combined experimental and dft approach, Inorg. Chem. 47 (23) (2008) 10971–10979.

[26] E. Oelkers, J.-M. Montel, Phosphates and nuclear waste storage, Elements 4 (2008) 113–116.

[27] F. Poitrasson, E. Oelkers, J. Schott, J.-M. Montel, Experimental determination of synthetic ndpo4 monazite end-member solubility in water from 21°c to 300°c: i Geochim. Cosmochim. Acta 68 (10) (2004) 2207 – 2221. `doi:http://dx.doi.org/10.1016/j.gca.2003.12.010`.
URL `http://www.sciencedirect.com/science/article/pii/S001670370300927X`

[28] B. E. Burakov, M. A. Yagovkina, V. M. Garbuzov, A. A. Kitsay, V. A. Zirlin, Self-irradiation of monazite ceramics: Contrasting behavior of PuPO$_4$ and (La,Pu)PO$_4$ doped with Pu-238, Mater. Res. Soc. Symp. P. 824 (2004) Mat Res Soc; SW Res Inst.

[29] D. Bregiroux, F. Audubert, T. Charpentier, D. Sakellariou, D. Bernache-Assollant, Solid-state synthesis of monazite-type compounds *Ln*PO$_4$ (*Ln*= La to Gd), Solid State Sci. 9 (5) (2007) 432–439. `doi:10.1016/j.solidstatesciences.2007.03.019`.

[30] N. Clavier, R. Podor, N. Dacheux, Crystal chemistry of the monazite structure, J. Eur. Ceram. Soc. 31 (6) (2011) 941–976. `doi:10.1016/j.jeurceramsoc.2010.12.019`.

[31] A. Meldrum, L. M. Wang, R. C. Ewing, Ion beam induced amorphization of monazite, Nucl. Instrum. Meth. B 116 (1) (1996) 220–224. `doi:10.1016/0168-583X(96)00037-7`.

[32] A. Meldrum, L. A. Boatner, L. M. Wang, R. C. Ewing, Ion-beam-induced amorphization of LaPO$_4$ and ScPO$_4$, Nucl. Instrum. Meth. B 127 (1997) 160–165. `doi:10.1016/S0168-583X(96)00873-7`.

[33] A. Meldrum, L. A. Boatner, R. C. Ewing, Displacive radiation effects in the monazite- and zircon-structure orthophosphates, Phys. Rev. B 56 (21) (1997) 13805–13814. `doi:10.1103/PhysRevB.56.13805`.

[34] A. Meldrum, L. A. Boatner, W. J. Weber, R. C. Ewing, Radiation damage in zircon and monazite, Geochim. Cosmochim. Acta 62 (14) (1998) 2509–2520. `doi:10.1016/S0016-7037(98)00174-4`.

[35] A. Meldrum, S. J. Zinkle, L. A. Boatner, R. C. Ewing, Heavy-ion irradiation effects in the ABO$_4$ orthosilicates: Decomposition, amorphization, and recrystallization, Phys. Rev. B 59 (6) (1999) 3981–3992. `doi:10.1103/PhysRevB.59.3981`.

[36] A. Meldrum, L. A. Boatner, R. C. Ewing, A comparison of radiation effects in crystalline ABO$_4$-type phosphates and silicates, Mineral. Mag. 64 (2) (2000) 185–194. `doi:10.1180/002646100549283`.

[37] A. Aloy, E. Kovarskala, T. Koltsova, S. Samoylov, G. Rovnyi, J. LJ, Immobilization of am-241, formed under plutonium metal conversion, into monazite-type cermaics, The 8th International Conference on Environmental Management (ICEM 2001).

[38] O. Terra, N. Dacheux, F. Audubert, R. Podor, Immobilization of tetravalent actinides in phosphate ceramics, J. Nucl. Mater. 352 (1-3) (2006) European Materials Res Soc. `doi:10.1016/j.jnucmat.2006.02.058`.

[39] O. Terra, N. Dacheux, N. Clavier, R. Podor, F. Audubert, Preparation of Optimized Uranium and Thorium Bearing Brabantite or Monazite/Brabantite Solid Solutions, J. Am. Ceram. Soc. 91 (11) (2008) 3673–3682. `doi:10.1111/j.1551-2916.2008.02678.x`.

[40] Y. X. Ni, J. M. Hughes, A. N. Mariano, Crystal-chemistry of the Monazite and Xenotime Structures, Am. Mineral. 80 (1-2) (1995) 21–26.

[41] W. Milligan, D. Mullica, G. Beall, L. Boatner, The structures of three lanthanide orthophosphates, Inorg. Chim. Acta 70 (0) (1983) 133 – 136. `doi:http://dx.doi.org/10.1016/S0020-1693(00)82791-7`.
URL `http://www.sciencedirect.com/science/article/pii/S0020169300827917`

[42] W. Milligan, D. Mullica, G. Beall, L. Boatner, Structures of erpo4, tmpo4, and ybpo4, Acta Crystallogr. C 39 (1) (1983) 23–24.

[43] W. Milligan, D. Mullica, G. Beall, L. Boatner, Structural investigations of YPO$_4$, ScPO$_4$, and LuPO$_4$, Inorg. Chim. Acta 60 (0) (1982) 39 – 43. `doi:http://dx.doi.org/10.1016/S0020-1693(00)91148-4`.
URL `http://www.sciencedirect.com/science/article/pii/S0020169300911484`

[44] R. Podor, M. Cuney, Experimental study of Th-bearing LaPO4(780 degrees C, 200 MPa): Implications for monazite and actinide orthophosphate stability, Am. Mineral. 82 (7-8) (1997) 765–771.

[45] R. Podor, M. Cuney, C. N. Trung, Experimental study of the solid solution between monazite-(La) and (Ca0.5U0.5)PO4 at 780 degrees C and 200 MPa, Am. Mineral. 80 (11-12) (1995) 1261–1268.

[46] R. S. de Biasi, A. A. R. Fernandes, J. C. S. Oliveira, Cell Volumes of LaPO$_4$-CePO$_4$ Solid-solutions, J. Appl. Crystallogr. 20 (1987) 319–320. `doi:10.1107/S0021889887086606`.

[47] O. Terra, N. Clavier, N. Dacheux, R. Podor, Preparation and characterization of lanthanum-gadolinium monazites as ceramics for radioactive waste storage, New J. Chem. 27 (6) (2003) 957–967. `doi:10.1039/b212805p`.

[48] K. Popa, R. J. M. Konings, T. Geisler, High-temperature calorimetry of (La$_{1-x}$Ln$_x$)PO$_4$ solid solutions, J. Chem. Thermodyn. 39 (2007) 236–239.

[49] A. Thust, Y. Arinicheva, E. Haussühl, J. Ruiz-Fuertes, L. Bayarjargal, S. C. Vogel, S. Neumeier, B. Winkler, Physical Properties of La$_{1-x}$Eu$_x$PO$_4$, $0 \leq x \leq 1$, Monazite-Type Ceramics, J. Am. Ceram. Soc. 98 (12) (2015) 4016–4021. `doi:10.1111/jace.13841`.

[50] P. Zeng, Y. Teng, Y. Huang, L. Wu, X. Wang, Synthesis, phase structure and microstructure of monazite-type Ce$_{1-x}$Pr$_x$PO$_4$ solid solutions for immobilization of minor actinide neptunium, J. Nucl. Mater. 452 (1) (2014) 407–413.

[51] Y. Arinicheva, A. Bukaemskiy, S. Neumeier, G. Modolo, D. Bosbach, Studies on thermal and mechanical properties of monazite-type ceramics for the conditioning of minor actinides, Prog.Nucl.Energ. 72 (2014) 144–148.

[52] F. Brandt, S. Neumeier, T. Schuppik, Y. Arinicheva, A. Bukaemskiy, G. Modolo, D. Bosbach, Conditioning of minor actinides in lanthanum monazite ceramics: a surrogate study with europium, Prog.Nucl.Energ. 72 (2014) 140–143.

[53] R. D. Shannon, Revised effective ionic radii and systematic studies of interatomic distances in halides and chalcogenides, Acta Crystallogr. A 32 (5) (1976) 751–767. `doi:10.1107/S0567739476001551`.
URL `http://dx.doi.org/10.1107/S0567739476001551`

[54] E. Jarosewich, L. Boatner, Rare-earth element reference samples for electron microprobe analysis, Geostandard. Newslett. 15 (2) (1991) 397–399.

[55] A. Hammersley, S. Svensson, M. Hanfland, A. Fitch, D. Hausermann, Two-dimensional detector software: from real detector to idealised image or two-theta scan, High Pressure Res. 14 (4-6) (1996) 235–248.

[56] H. M. Rietveld, Line profiles of neutron powder-diffraction peaks for structure refinement, Acta Crystallogr. 22 (1) (1967) 151–152. `doi:10.1107/S0365110X67000234`.

URL `http://dx.doi.org/10.1107/S0365110X67000234`

[57] A. Coelho, Topas V 2.0: General profile and structure analysis software for powder diffraction data. (2000).

[58] P. Thompson, D. E. Cox, J. B. Hastings, Rietveld refinement of Debye–Scherrer synchrotron X-ray data from $\mathrm{Al_2O_3}$, J. Appl. Crystallogr. 20 (2) (1987) 79–83. `doi:10.1107/S0021889887087090`.
URL `http://dx.doi.org/10.1107/S0021889887087090`

[59] OriginLab, Origin, OriginLab, Nothampton, MA, n.d.

[60] A. Navrotsky, Progress and new directions in high temperature calorimetry, Phys. Chem. Miner. 2 (1-2) (1977) 89–104.

[61] A. Navrotsky, Progress and new directions in high temperature calorimetry revisited, Phys. Chem. Miner. 24 (3) (1997) 222–241.

[62] A. Navrotsky, Progress and new directions in calorimetry: A 2014 perspective, J. Am. Ceram. Soc. 97 (11) (2014) 3349–3359.

[63] S. V. Ushakov, K. B. Helean, A. Navrotsky, L. A. Boatner, Thermochemistry of rare-earth orthophosphates, J. Mater. Res. 16 (9) (2001) 2623–2633. `doi:10.1557/JMR.2001.0361`.

[64] D. Mullica, W. Milligan, D. A. Grossie, G. Beall, L. Boatner, Ninefold coordination $\mathrm{LaPO_4}$: Pentagonal interpenetrating tetrahedral polyhedron, Inorg. Chim. Acta 95 (4) (1984) 231 – 236. `doi:http://dx.doi.org/10.1016/S0020-1693(00)87472-1`.
URL `http://www.sciencedirect.com/science/article/pii/S0020169300874721`

[65] L. Vegard, H. Dale, Untersuchungen über mischkristalle und legierungen, Z. Kristallogr. 67 (1928) 148–162.

[66] N. Kitamura, K. Amezawa, Y. Tomii, N. Yamamoto, T. Hanada, Protonic conduction in Sr-doped $(\mathrm{La}_{1-x}\mathrm{Sm}_x)\mathrm{PO}_4$, Solid State Ionics 175 (1–4) (2004) 563 – 567, fourteenth International Conference on Solid State Ionics. `doi:10.1016/j.ssi.2004.02.077`.
URL `http://www.sciencedirect.com/science/article/pii/S016727380400668X`

[67] D. F. Mullica, D. A. Grossie, L. A. Boatner, Coordination Geometry and Structural Determinations of $\mathrm{SmPO_4}$, $\mathrm{EuPO_4}$ and $\mathrm{GdPO_4}$, Inorg. Chim. Acta 109 (2) (1985) 105–110. `doi:10.1016/S0020-1693(00)84549-1`.

[68] D. F. Mullica, D. A. Grossie, L. A. Boatner, Structural Refinements of Praseodymium and Neodymium Orthophosphate, J. Solid State Chem. 58 (1) (1985) 71–77. `doi:10.1016/0022-4596(85)90269-5`.

[69] D. Mullica, E. Sappenfield, L. Boatner, A structural investigation of several mixed lanthanide orthophosphates, Inorg. Chim. Acta 174 (2) (1990) 155 – 159. `doi:http://dx.doi.org/10.1016/S0020-1693(00)80293-5`.
URL `http://www.sciencedirect.com/science/article/pii/S0020169300802935`

[70] A. Hezel, S. Ross, Forbidden transitions in the infra-red spectra of tetrahedral anions – III. Spectra-structure correlations in perchlorates, sulphates and phosphates of the formula $\mathrm{MXO_4}$, Spectrochim. Acta 22 (11) (1966) 1949–1961.

[71] L. Chun-hua, H. Jie, X. Zhongzi, N. Yaru, Preparation and IR spectra study of rare earth orthophosphates, J. Rare Earth. 25 (2007) 273–276.

[72] K. Ruschel, L. Nasdala, A. Kronz, J. M. Hanchar, D. M. Tobbens, R. Skoda, F. Finger, A. Moller, A Raman spectroscopic study on the structural disorder of monazite-(Ce), Miner. Petrol. 105 (1-2) (2012) 41–55. `doi:10.1007/s00710-012-0197-7`.

[73] G. M. Begun, G. W. Beall, L. A. Boatner, W. J. Gregor, Raman-spectra of the Rare-earth Orthophosphates, J. Raman Spectrosc. 11 (4) (1981) 273–278. `doi:10.1002/jrs.1250110411`.

[74] D. E. Hobart, G. M. Begun, R. G. Haire, H. E. Hellwege, Raman-spectra of the Transplutonium Ortho-phosphates and Trimetaphosphates, J. Raman Spectrosc. 14 (1) (1983) 59–62. `doi:10.1002/jrs.1250140114`.

[75] R. Podor, Raman spectra of the actinide-bearing monazites, Eur. J. Mineral. 7 (6) (1995) 1353–1360.

[76] C. Santos, E. Silva, A. Ayala, I. Guedes, P. Pizani, C.-K. Loong, L. A. Boatner, Raman investigations of rare earth orthovanadates, J. Appl. Phys. 101 (5) (2007) 053511.

[77] J. Cheng, A. Navrotsky, Enthalpies of Formation of $\mathrm{LaBO_3}$ Perovskites (B= Al, Ga, Sc, and In), J. Mater. Res. 18 (10) (2003) 2501–2508.

[78] R. Robie, B. Hemingway, J. Fisher, Thermodynamic properties of minerals and related substances at 298.15 K and 1 bar (10^5 Pascals) pressure and at higher temperatures, U.S. Geol. Survey Bull. 1452 (1979) 456.